

CsPbBr₃ Nanocrystal Films: Deviations from Bulk Vibrational and Optoelectronic Properties

Silvia G. Motti, Franziska Krieg, Alexandra J. Ramadan, Jay B. Patel, Henry J. Snaith, Maksym V. Kovalenko, Michael B. Johnston, and Laura M. Herz*

Metal-halide perovskites (MHP) are highly promising semiconductors for light-emitting and photovoltaic applications. The colloidal synthesis of nanocrystals (NCs) is an effective approach for obtaining nearly defect-free MHP that can be processed into inks for low-cost, high-performance device fabrication. However, disentangling the effects of surface ligands, morphology, and boundaries on charge-carrier transport in thin films fabricated with these high-quality NCs is inherently difficult. To overcome this fundamental challenge, terahertz (THz) spectroscopy is employed to optically probe the photoconductivity of CsPbBr₃ NC films. The vibrational and optoelectronic properties of the NCs are compared with those of the corresponding bulk polycrystalline perovskite and significant deviations are found. Charge-carrier mobilities and recombination rates are demonstrated to vary significantly with the NC size. Such dependences derive from the localized nature of charge carriers within NCs, with local mobilities dominating over interparticle transport. It is further shown that the colloiddally synthesized NCs have distinct vibrational properties with respect to the bulk perovskite, exhibiting blue-shifted optical phonon modes with enhanced THz absorption strength that also manifest as strong modulations in the THz photoconductivity spectra. Such fundamental insights into NC versus bulk properties will guide the optimization of nanocrystalline perovskite thin films for optoelectronic applications.

Perovskite NCs show high photoluminescence quantum yields (PLQY) and tunable band gap over all the visible range, among other desirable properties for light-emitting applications.^[1–3] The fabrication of high-quality conductive thin films by processing the colloidal NCs as inks has paved the way for an extension of their application to photovoltaics and photodetectors.^[4,5] However, the long-range electronic conductivity of these nanocrystalline thin films depends crucially on interparticle conduction and thus should be greatly affected by the choice of ligands and deposition methods.^[5,6] Such insulating ligands may form barriers between the semiconducting NCs and metallic electrodes that hamper charge transport in devices.


While the optimization of long-range conductivity is a developing topic with its own ongoing efforts, the investigation of the fundamental charge transport within individual NCs is also crucial, since both intra- and interparticle charge motions will affect the performance of perovskite

1. Introduction

The colloidal synthesis of metal halide perovskite (MHP) semiconductor nanocrystals (NCs) has proven to be an interesting and effective approach for yielding nearly defect-free materials.

Dr. S. G. Motti, Dr. A. J. Ramadan, Dr. J. B. Patel,
Prof. H. J. Snaith, Prof. M. B. Johnston, Prof. L. M. Herz
Department of Physics
University of Oxford
Clarendon Laboratory
Parks Road, Oxford OX1 3PU, UK
E-mail: laura.herz@physics.ox.ac.uk

F. Krieg, Prof. M. V. Kovalenko
Institute of Inorganic Chemistry
Department of Chemistry and Applied Biosciences
ETH Zürich
Vladimir Prelog Weg 1, Zürich CH-8093, Switzerland
F. Krieg, Prof. M. V. Kovalenko
Laboratory for Thin Films and Photovoltaics
Empa–Swiss Federal Laboratories for Materials Science and Technology
Überlandstrasse 129, Dübendorf CH-8600, Switzerland

 The ORCID identification number(s) for the author(s) of this article can be found under <https://doi.org/10.1002/adfm.201909904>.

DOI: 10.1002/adfm.201909904

NC devices. In addition, an understanding of the interplay between electronic confinement and charge transport is important for the design of NC solids that can still fully exploit the size-dependent band gap tunability. Previous studies showed that appreciable conductivity can be achieved from perovskite NC films with the use of short capping ligands (chains of eight carbons or less) or by removal/exchange of ligands after film deposition.^[4,7,8] While these approaches facilitate interparticle charge transport, they also lead to partial sintering of NCs,^[9] which in turn is expected to result in loss of quantum confinement and higher density of structural defects. Such effects may be particularly undesirable for light-emitting applications, while they may potentially be more tolerable for photovoltaic devices. The development of zwitterionic ligands has been proposed as an effective approach to obtain stable colloidal NCs and allowing for the deposition of smooth conductive films while preserving NC structural integrity.^[5] Zwitterionic ligands may, therefore, be particularly suitable for balancing the trade-off between preserving nanocrystalline optoelectronic properties and maintaining effective charge-carrier transport.

In this work, we investigate the vibrational and optoelectronic properties of colloiddally synthesized cuboid CsPbBr₃ NCs of edge lengths 6, 7.5, and 10 nm deposited on quartz

substrates. Such NCs fall within the range of weak quantum confinement, approaching bulk-like properties with increasing crystal size. Furthermore, the synthesis of NCs in this range of sizes yields optimum crystal quality and colloidal stability. To investigate the effects of nanoscale interfaces, we compare our findings with those for a spin-coated polycrystalline CsPbBr₃ film exhibiting average crystallite size of ≈100 nm. We apply a combination of absorption and PL studies with optical-pump terahertz-probe (OPTP) spectroscopy to unravel the charge-carrier dynamics and photoconductivity in the perovskite NCs and bulk films. The THz radiation can access the energy and time scales of charge-carrier motion and lattice vibrations that can affect charge transport. Moreover, the THz probe allows us to optically measure the time-resolved photoconductivity of the material after photoexcitation without the need for electrical contacts.^[10–13]

Our findings reveal distinct structural and vibrational properties in NCs compared to the bulk material. We observe a blue-shift of the optical phonon modes probed in the THz spectral range and stronger coupling of the THz radiation to these modes with respect to the bulk. In addition to wider band gaps and higher recombination rates resulting from quantum confinement, we also report a size dependence of the effective charge-carrier mobilities. We demonstrate that the charge transport within the NCs in the THz frequency is dominated by backscattering off NC boundaries, even after film annealing, highlighting the dominance of intra- over interparticle transport in these NC solids. These two aspects, the localized character of charge carriers and the distinct vibrational properties of NCs, are reflected in the frequency dependence of the THz photoconductivity spectra. In particular, upon photoexcitation, we observe a modification of the phonon response, which results in strong modulations on the photoconductivity spectra. These photoinduced changes are also enhanced in the NCs with respect to the bulk, reflecting the stronger coupling of the polar lead-bromide sublattice to the THz probe.

2. Results and Discussion

2.1. Sample Fabrication and Characterization

Cuboid-shaped CsPbBr₃ NCs of average sizes 6, 7.5, and 10 nm were synthesized colloidally, using a hot-injection approach. Anhydrous cesium oleate, lead oleate, and zwitterionic ligand were dissolved in 1-octadecene and heated under vacuum to 130 °C after which the atmosphere was changed to nitrogen. Once the desired reaction temperature was reached, trioctylphosphine adduct was injected and the reaction was cooled to room temperature immediately thereafter; an ice-water bath was used. Full details of the synthesis, isolation, and purification procedures are provided in Section 1, Supporting Information. The sizes (edge lengths) of the NCs determined by transmission electron microscopy (TEM) were 6 ± 2, 7.5 ± 2, and 10 ± 2 nm. The PLQY values measured for NCs in colloidal solutions were 67%, 75%, and 75%, respectively. For the fabrication of NC films, the NCs were deposited on z-cut quartz substrates^[14] by spin coating from the colloidal solution. After deposition, the measured PLQY on the films were slightly reduced, to 50%,

47%, and 26%, for the 6, 7.5, and 10 nm NCs, respectively. The center wavelength of the PL emission did not change after deposition, indicating preservation of confinement, and hence preservation of the structural integrity of the NCs.

For comparison with bulk perovskite properties, bulk polycrystalline CsPbBr₃ films were fabricated by spin coating of a Cs-Pb-Br-precursor solution in dimethyl sulfoxide onto the quartz substrates at 4000 rpm for 40 s followed by a solvent annealing step using chloroform (for more details, see Section 1.5, Supporting Information). The average crystallite size within the bulk film was ≈100 nm as determined by atomic force microscopy (Figure S12, Supporting Information).

As a first characterization step, absorption and PL spectra were taken, as shown in Figure 1a. As expected, with decreasing crystal size, the NCs show an increasing blue shift of the absorption onset and the PL peak position with respect to the data for the bulk CsPbBr₃ film, confirming the presence of weak confinement.^[1] We also note a broadening of the PL emission and the excitonic feature in the absorption spectra of the NC films with respect to those of the bulk thin film. Such broadening is related to the size distribution (±1–2 nm, see Figures S12 and S13, Supporting Information) of the NCs, and more pronounced in the case of the smaller NCs.

2.2. Size Dependence of Structural and Vibrational Properties

The low dimensionality and the high surface-to-volume ratio of semiconductor NCs have been shown to have an effect on their crystal lattice.^[15–17] To investigate such effects, we examined the structural properties of the bulk and nanocrystalline perovskite films by X-ray diffraction (XRD). The diffraction patterns obtained for the polycrystalline CsPbBr₃ and 10 nm NCs deposited on quartz are shown in Figure 1b (see Figure S7, Supporting Information, for complete diffraction data for all NC sizes). No peaks related to PbBr₂ or other impurities were detected. We observe broadening of the diffraction peaks with decreasing crystal size, as is typical in NCs.^[18,19] Interestingly, we can also notice a shift of the diffraction peaks to lower angles with respect to the bulk CsPbBr₃. Such a shift is related to longer distances between planes, and usually associated with lattice strain.^[20] In order to properly analyze the position and broadening of the diffraction peaks, we must take into account the crystalline phase and peak superpositions. It has been shown that CsPbBr₃ NCs fabricated from colloidal synthesis adopt an orthorhombic structure, analogous to the bulk material.^[21,22] According to the expected diffraction pattern for orthorhombic CsPbBr₃,^[23] we fitted the peaks and calculated the d-spacings for the (101), (121), and (202) planes and noticed that the NC films exhibit slightly but consistently larger plane distances than the bulk perovskite (see Figure S8, Supporting Information). We then used the fitted peak positions and broadenings to create Williamson–Hall plots^[24] for bulk and NC films and found no significant presence of microstrain (see Figure S10, Supporting Information), suggesting good crystallite quality and insignificant defect-related distortion. Considering the negligible contribution of microstrain and inhomogeneities, the increased d-spacings indicate a lattice expansion in the NCs with respect to the bulk. The expansion

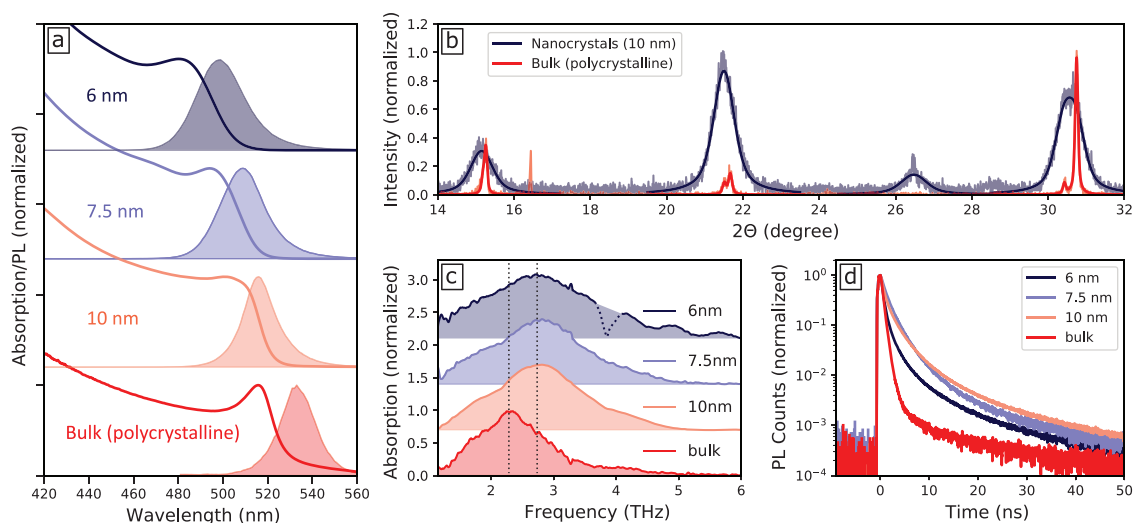


Figure 1. a) Absorption and PL spectra of CsPbBr₃ nanocrystals (average size 6, 7.5, and 10 nm) deposited on quartz substrates and spin coated polycrystalline film (average grain size ≈ 100 nm). b) XRD diffraction patterns obtained from the 10 nm nanocrystals and the spin coated polycrystalline film, corrected for tilting according to the quartz substrate diffraction peaks as reference. c) Normalized THz absorption spectra in the dark for the nanocrystals and the spin coated polycrystalline film; offsets were added for clarity; the dashed line in the 6 nm NC spectrum is an artifact caused by the absorption of the quartz substrate,^[14] visible in the cases of films with lower optical density. d) PL decay dynamics of polycrystalline and nanocrystalline CsPbBr₃ obtained at excitation fluence ≈ 20 nJ cm⁻², wavelength 398 nm, 5 MHz repetition rate.

of the lattice in NCs has been previously reported in different systems,^[15,25,26] including lead halide perovskites,^[16,27] and has been attributed to a decrease in electrostatic forces between the atoms induced by the reduced valence of atoms at the NC surfaces.^[26]

The differences in lattice expansion combined with reduced particle size and high surface-to-volume ratio is expected to have an effect on the vibrational properties of semiconductor NCs.^[15,28] To elucidate such effects, we investigated the optical phonon modes associated with the lead-bromide sublattice in both the NCs and bulk CsPbBr₃ by measuring the absorption of the films in the THz region. As Figure 1c shows, the THz absorption spectra of the NCs are broader and the modes appear to be blue-shifted compared to those of the bulk. We propose that such broadening of the phonon modes in the NCs is related to shorter phonon lifetimes (given the energy-time uncertainty relation $\Delta E/\hbar = 1/\tau$) that result from confinement effects and increased surface scattering in NCs.^[15,29] The broadening of the THz absorption increases with decreased NC size (see Figure S14, Supporting Information), which directly implies a decrease of the phonon lifetime in smaller NCs.

Regarding the blue-shift of the THz spectra, the absence of size dependence between NCs suggests that phonon confinement is not the dominant cause of the shift over the studied size range. Intriguingly, the lattice expansion observed for the NCs in the XRD patterns also fails to explain the blue-shift of the optical phonon modes, given that the reduced electrostatic force is expected to induce a softening of the phonon modes (i.e., red-shift) instead of the observed blue-shift. We, therefore, propose that the observed effect may instead derive mostly from changes in the direct coupling of radiation across the multitude of optical phonon modes that is present in lead halide perovskites,^[30,31] which have numerous atoms per unit cell leading to the existence of many acoustic and optical modes. In support

of this conclusion, we note that the relative effective absorption coefficients of the phonon modes (obtained by comparing the absorption in the THz region relative to the edge of the optical gap) are higher by a factor of 2 in the NCs compared to the bulk (see Figure S15, Supporting Information). This more efficient coupling of the lattice modes to THz radiation can be a result of distinct selection rules in NC films or distinct phonon distributions, and has an effect on the THz photoconductivity spectra, as we will discuss in Section 2.4 further below. Such changes, therefore, suggest that the perceived blue-shift of optical phonon modes in the NCs may derive from complex changes to the vibrational frequencies and coupling strengths of optical modes to infrared radiation. We note that since significant broadening of the optical modes persists even at low temperature (Figure S16, Supporting Information), individual phonon modes could not be resolved.

The higher absorption coefficients and blue shift of the phonon modes in NCs reveal the distinct vibrational properties of NCs with respect to the bulk. In addition, the lack of size dependence of the optical phonon mode absorption fingerprint (Figure 1c) indicates that the fabrication methods might also play a role in determining surface and morphological properties.

2.3. Charge-Carrier Dynamics

In addition to wider band gaps and structural variations, another characteristic effect of confinement commonly observed in semiconductor NCs is higher charge-carrier recombination rates with decreasing size.^[32,33] To investigate the size dependence of charge-carrier dynamics in CsPbBr₃, we first measured the transient PL decays of the bulk and NC films, following photoexcitation with 3.1 eV ($\lambda = 400$ nm) photons. As

can be observed in Figure 1d, the polycrystalline bulk CsPbBr₃ film shows shorter PL lifetimes than the NC films, which can be attributed to the high prevalence of defects in polycrystalline lead bromide perovskite films.^[34–36] While the higher surface-to-volume ratio in NCs is associated with a higher density of boundaries and dangling bonds, the attached ligands effectively passivate the crystal surfaces,^[37] ultimately resulting in a lower defect density with respect to the bulk. It can also be observed that the smaller NCs show shorter PL lifetimes than larger NCs. Given that the PLQY values were similar or higher for smaller crystals, the shorter PL lifetimes for smaller NCs must be associated with higher radiative rates. No significant fluence dependence was observed in the PL dynamics (see Figure S17, Supporting Information) at these excitation densities, indicating a predominance of a monomolecular recombination mechanism. Given that rates appear to be dominated by a radiative mechanism, we therefore suggest that this monomolecular mechanism is to a large extent associated with excitonic recombination. We assume, however, that both excitons and free carriers can coexist in the material. In the case of NCs at these low excitation fluences (between 1 and 100 nJ cm⁻²), we estimate that an average of less than 0.02 photoexcitations are initially generated per crystal (for details, see Section 4, Supporting Information), which explains the absence of any high-order effects. However, we note that instead of monoexponential (first-order) decays intuitively expected from monomolecular recombination, all NCs present fairly stretched PL dynamics. Such complex dynamics are most likely associated with inhomogeneities of size distribution, photon reabsorption, and charge diffusion between NCs in the film.^[11,38–40]

To investigate higher-order charge-carrier recombination processes across a wider range of carrier densities and with higher time resolution, we performed OPTP spectroscopy for the range of NC sizes allowing us to probe the transient photoconductivity of the films following pulsed photoexcitation. The THz radiation is a non-contact probe sensitive to the photo-generated charge-carrier population density and the effective charge-carrier mobility (for details, see Section 3, Supporting Information),^[10,12] making it ideal for the study of NC films, for which the insulating ligands and contact barriers would greatly affect the results obtained from electrical measurements. The measurements were performed with photoexcitation by 35 fs pulses of 3.1 eV ($\lambda = 400$ nm) photons for a range of different excitation fluences. The transients were fitted with a dynamic model that describes the charge-carrier population decay with a combination of first-, second-, and third-order recombination rates, with rate constants k_1 , k_2 , and k_3 , respectively (for details, see Section 1.5.1, Supporting Information).^[10,12,13] Figure 2 shows the OPTP dynamics obtained from the NCs of different sizes together with best fits based on this model. We were able to obtain good-quality fits assuming a negligible first-order rate constant k_1 (which relates to a combination of excitonic and nonradiative recombination pathways) in agreement with the observation of flat photoconductivity decay at the lowest fluences. The absence of first-order recombination can be explained by the 1 ns time window over which the OPTP transients are recorded, which is significantly shorter than the approximate first-order decay constant ($\tau \approx 4$ ns) describing the initial decay of the PL transients. Therefore, monomolecular

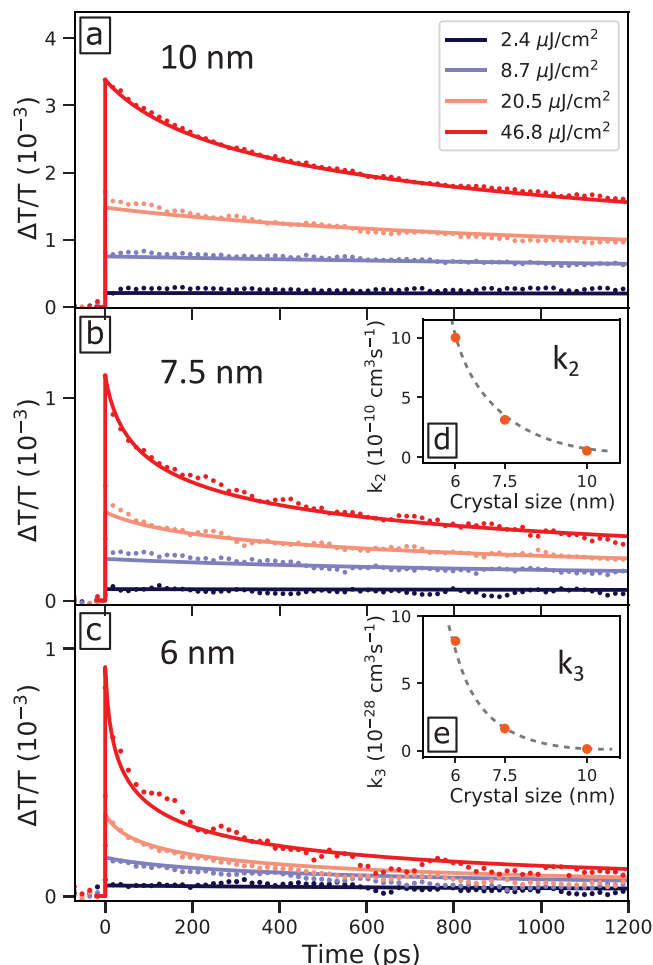


Figure 2. Photoconductivity dynamics (plotted as $-\Delta T_{\text{THz}}/T_{\text{THz}} \propto \sigma$; excitation at 400 nm, repetition rate 5 kHz) of CsPbBr₃ nanocrystals of average size of a) 10, b) 7.5, and c) 6 nm deposited on quartz. Dots are experimental data and solid lines are the rate equation fits to the fluence dependence as described in detail in Section 1.5.1, Supporting Information. Insets show the fitted values of rate constants d) k_2 and e) k_3 . Dashed gray lines are guides to the eye.

recombination has little influence on the shape of the OPTP transients.

Given the higher fluences employed during the OPTP measurements, the estimated carrier densities suggest the presence of more than one excitation per crystal with increasing fluences (for details, see Section 4, Supporting Information). In such cases, we expect higher contributions from second- and third-order (k_2 and k_3) recombination processes. The values for the effective rate constants k_2 and k_3 extracted from these fits are shown in Figure 2d,e, which highlight notable increases in both k_2 and k_3 with decreasing NC size. Such higher recombination rate constants may result from the stronger overlap of electron and hole wave functions caused by confinement effects,^[41,42] which results from a combination of confinement-induced state mixing, enhanced Coulomb coupling, and increasing surface-to-volume ratio.^[43] In addition, these values may be affected by increasing excitonic effects with decreasing NC size because the values of k_2 and k_3 determined in OPTP are factored with

the photon-to-charge branching ratio, which may increase with increasing exciton-binding energy (for details, see Section 3, Supporting Information).

2.4. Charge-Carrier Mobility and Localization

We may further examine how charge-carrier confinement in the NCs affects the effective charge-carrier mobility by evaluating the differential THz transmission ($-\Delta T_{\text{THz}}/T_{\text{THz}}$) amplitude immediately after photoexcitation. The magnitude of the $-\Delta T_{\text{THz}}/T_{\text{THz}}$ signal is proportional to photoinduced conductivity and therefore the product of the charge-carrier mobility μ and the charge-carrier population. We are, thus, able to determine an effective charge-carrier mobility $\phi\mu$ from the initial photoconductivity signal immediately after excitation, before significant charge-carrier recombination has occurred. Here, ϕ is the photon-to-charge-carrier generation ratio, which accounts for the unknown conversion factor of photons absorbed to charge-carriers generated (for details, see Section 3, Supporting Information)^[10,12] and μ is the sum of the electron and hole mobilities. As shown in Figure 3a, the effective $\phi\mu$ values obtained for the 10, 7.5, and 6 nm NCs decrease with decreasing crystal size from 2.8 to 0.7 $\text{cm}^2 \text{V}^{-1} \text{s}^{-1}$, indicating increasing localization of charge carriers within the confines of the NCs. We note that such a reduction in $\phi\mu$ can be the result of both increasing excitonic effects (decreasing ϕ) and increasing proximity of physical barriers (decreasing μ) with decreasing NC size.

To investigate further why the NC size has an effect on the effective charge-carrier mobilities, we examined the influence of ligands and how the barriers between NCs affect charge-carrier localization. We obtained the effective terahertz mobilities of NC films of one particular size (7.5 nm) but prepared with different ligands. Ligand 1 is the C3 sulfobetaine system (3-(*N,N*-dimethyloctadecylammonio)propanesulfonate) used in the samples presented so far. Ligand 2, lecithin, has twice as many tails per head group at similar surface ligand density, thus resulting in more effective insulation between crystals. The films with ligand 3 were obtained by solid-state ligand exchange with a di-zwitterionic ligand (3,3'-(hexane-1,6-diylbis(dimethylammoniumdiyl))bis propane-1-sulfonate) and are expected to be less insulating than the ligands 1 and 2 (for details, see Section 1.1, Supporting Information). As Figure 3b indicates, no significant difference in effective charge-carrier mobility with ligand type was observed. We then subjected one film of 7.5 nm NCs with ligand 1 to annealing at 150 °C for 10 min. We observed a red shift of the optical band gap (see Figure S19, Supporting Information) following annealing, evidencing loss of confinement due to ligand extraction and/or merging of crystals. Surprisingly, however, no significant increase of effective mobility was observed (Figure 3b). Taken together, these observations demonstrate that the effective THz mobilities of NC films are dominated by intra-NC motion of charge carriers, rather than migration between NCs. While interparticle charge-carrier diffusion probably does occur (as indicated by the stretched PL decays and long-range photoconductivity in these films^[5]), we suggest that the associated interparticle mobility of charge carriers is still substantially lower

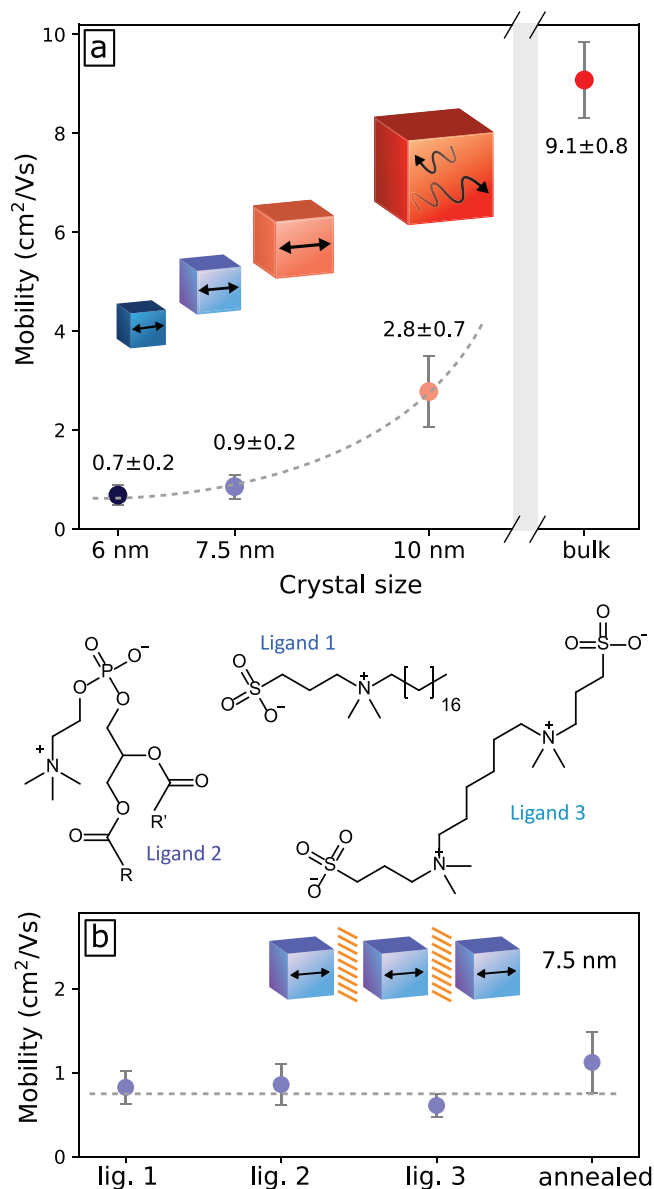


Figure 3. a) Size dependence of the effective THz mobilities obtained from OPTP measurements on deposited nanocrystals and b) effective THz mobilities of 7.5 nm crystals with different ligands and after annealing at 150 °C for 10 min. The molecular structures of the ligands are shown in the middle panel, where R and R' can be different saturated or unsaturated 16- or 18-carbon long carbo-hydrate chains (for more details, see Section 1, Supporting Information).

than the intra-particle mobility. As a result, the measured effective THz mobility mostly reflects carrier motion within individual particles, which is limited by the boundaries of the NCs. We note that such observations (of significantly larger high-frequency than low-frequency carrier mobility) have also been typical of metal oxide nanoparticle films.^[44]

We also investigated the charge-carrier mobility for the CsPbBr₃ bulk polycrystalline film for comparison and obtained a value of $\phi\mu = 9.1 \text{ cm}^2 \text{V}^{-1} \text{s}^{-1}$, similar to that determined elsewhere for lead bromide perovskite films^[12] with a range of A-cation choices. While this effective mobility is higher

than that measured for the larger NCs, it is significantly lower than the theoretically predicted upper limit for mobility of $\approx 200 \text{ cm}^2 \text{ V}^{-1} \text{ s}^{-1}$ (or $400 \text{ cm}^2 \text{ V}^{-1} \text{ s}^{-1}$ when probing the sum of electron and hole mobilities, such as in our case) for CsPbBr_3 expected for the case when only Fröhlich interactions with longitudinal phonons are operational.^[45,46] Given that the measured mobility does not vary with excitation fluence (see Figure S20, Supporting Information), we can disregard the contribution of carrier-carrier scattering. We, therefore, infer that the charge-carrier mobility in the polycrystalline film investigated here is limited by carrier scattering with defects, which may include grain boundaries that could potentially have an effect analogous to that of the surfaces of NCs.

To investigate whether the mechanisms leading to carrier scattering in NCs films differ from those limiting charge-carrier mobilities in the bulk polycrystalline films, we investigate the frequency dependence of the photoconductivity. Photoconductivity spectra are able to differentiate cleanly between strong localization effects and random scattering events on charge-carrier motion. In the case of random scattering events, the complex conductivity (σ) of metals and semiconductors under an alternating electric field of frequency ω can usually be described by the Drude model as

$$\sigma(\omega) = \frac{Ne^2}{m^*} \frac{i}{\omega + i\gamma} \quad (1)$$

where m^* is the charge-carrier effective mass and γ is the scattering rate, which relates to the mobility μ by

$$\mu = \frac{e}{m^* \gamma} \quad (2)$$

This model assumes a simple acceleration of a charge carrier in an electric field subject to its momentum being randomized through scattering events at average time intervals $1/\gamma$. Figure 4a shows the complex THz photoconductivity spectrum of a bulk CsPbBr_3 film taken ≈ 20 ps after photoexcitation. No spectral variations over time delay were found to occur (Figures S23 and S24, Supporting Information). The solid lines are spectra simulated with the Drude model according to Equation (1) considering the effective mass for electrons and holes to be $0.15 m_e$ ^[1] and fixing the scattering rate according to the experimentally measured value for the effective mobility in the bulk polycrystalline CsPbBr_3 of $9.1 \text{ cm}^2 \text{ V}^{-1} \text{ s}^{-1}$. Despite some modulations in the spectra, the photoconductivity of the bulk perovskite shows good agreement with the Drude model, displaying a positive real, and a near-zero imaginary part of the spectrum.

The frequency-dependent photoconductivity of the NCs (Figure 4b), on the other hand, deviates strongly from such Drude-like spectra. We observe that the conductivity at low frequency, instead of reaching a maximum, as expected from the Drude model, tends to zero in the case of the NCs. This is a common observation in semiconductor nanoparticles and can be associated with charge-carrier localization, where the presence of barriers significantly reduces the DC conductivity.^[47–50] Another striking characteristic of this behavior is the negative imaginary part of the spectra. One approach for evaluating

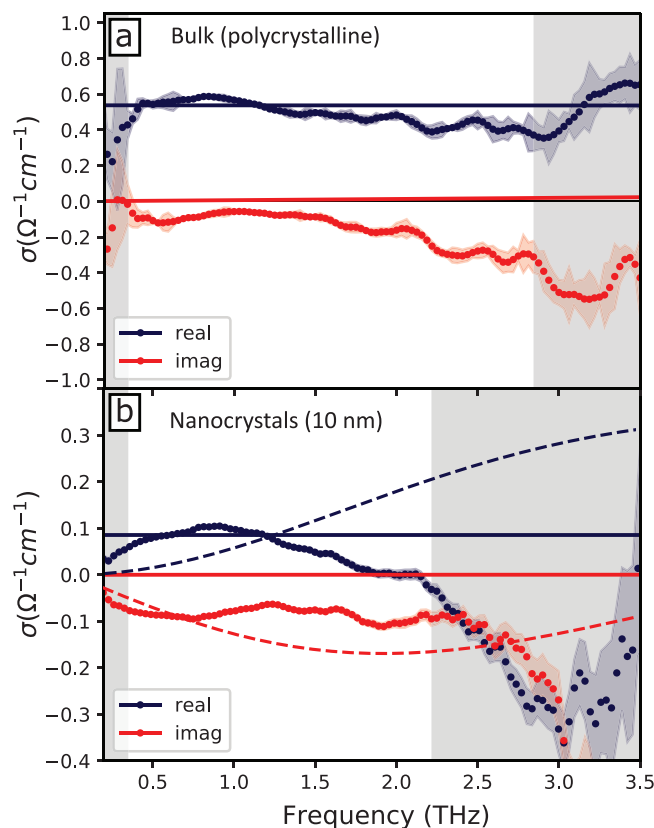


Figure 4. Real (dark blue) and imaginary (red) parts of THz photoconductivity spectra of a) a polycrystalline thin film and b) 10 nm nanocrystals of CsPbBr_3 deposited on quartz, ≈ 20 ps after photoexcitation at fluence $\approx 40 \mu\text{J cm}^{-2}$. Dots are experimental data while solid lines are simulated spectra from the Drude model and the dashed lines in panel (b) are obtained with Drude–Smith. The gray shaded areas mark regions of lower confidence (at frequencies lower than 0.35 THz due to focusing artifacts and in regions where the THz transmission is reduced by 90%). See Figure S22, Supporting Information, for other NC sizes.

this deviation from Drude behavior is by calculating the Drude quality factor f_{Drude} , which essentially compares the absolute magnitudes of the real and imaginary parts of the complex THz spectra (as described by Milot et al.^[51]). While $f_{\text{Drude}} = 1$ indicates ideal Drude behavior, deviations are indicated by values lower than 1. The values for f_{Drude} obtained from the THz spectra up to 2 THz are 0.97 for the bulk film and 0.58 for the NC film. These values demonstrate the difference in charge transport mechanism between the two cases and the localized nature of carriers in the NC film. We consider two models that are typically able to reproduce such behavior. First, we may investigate an exclusively excitonic character of the photoexcited carriers in the NCs and describe the frequency dependence of the THz photoconductivity as a Lorentz oscillator. In this case, a maximum of the real photoexcited THz spectra and a zero-crossing of the imaginary part would correspond to an intra-excitonic transition resonance which is directly related to the exciton binding energy.^[52] We are unable to observe any zero-crossing in the imaginary part of the spectra obtained from the NCs within the 3.5 THz range over which the spectra are recorded. However, this absence of an observable

resonance peak and crossing may potentially derive from the exciton binding energy being larger than 20 meV,^[52] in which case these intra-excitonic absorption features would fall outside our observation window. Since relatively large exciton binding energies have been observed for lead bromide perovskites, and electronic confinement will enhance these further,^[53–56] a clear resonance would therefore not be expected to fall within our observation window. However, the spectra could still be influenced by the low-frequency tail of such an excitonic response.

As a second example of a localized response, we consider the Drude–Smith model,^[50,57] a phenomenological adaptation of the Drude model that accounts for backscattering to reproduce the behavior of localized charge-carriers (see Section 1.5, Supporting Information). The Drude–Smith model extends the Drude model by considering scattering anisotropy according to

$$\sigma(\omega) = \frac{Ne^2}{m^*} \frac{i}{\omega + i\gamma} \left[1 + \sum_{p=1}^{\infty} \frac{c_p}{(1 - i\omega/\gamma_{DS})^p} \right] \quad (3)$$

where γ_{DS} is the Drude–Smith scattering rate, p is the number of scattering events, and c_p is the fraction of the initial velocity retained by carriers after each scattering event. For Drude-like photoconductivity, $c_p = 0$. In systems where charges are localized, c_p can be negative (from 0 to -1), representing preferential backwards scattering (for details, see Section 3.2, Supporting Information). Upon attempting to fit a Drude–Smith expression according to Equation (3) to the photoconductivity spectra of the NC films, we find adequate agreement with the data only for the low-frequency range (<1 THz). Furthermore, c_p tends toward -1 , indicating strong charge-carrier localization effects (Figure 4 shows a Drude–Smith spectrum for $c_p = -1$ as a dashed line). We note that while an intrinsic charge-carrier mobility value μ_{DS} can in principle be extracted from the Drude–Smith model according to $\mu_{DS} = (1 + c_p) \frac{e}{m^* \gamma_{DS}}$, in the limit of $c_p = -1$, this value will tend to infinity. Therefore, in cases of strong carrier localization, such as the NCs presented here, such derivations of intrinsic charge-carrier mobilities that could be attained in the absence of carrier backscattering off NC surfaces would be largely overestimated and are, therefore, avoided here.

The experimental photoconductivity spectrum from the NC film shows clear evidence of charge localization on the low-frequency side, which qualitatively agrees with the Drude–Smith model. However, it deviates from both the Drude model and the Drude–Smith model at higher frequencies, where it is affected by very strong modulations. The line-shape of the experimental spectra and the deviations from the theoretical predictions are not representative of charge transport phenomena, but rather of the combined interaction of the THz probe beam with the lattice and with the charge-carrier population. The response of the THz probe to charge-carrier motion is superimposed with modulations of the THz transmission caused by photoinduced changes to the lattice component in the absorption of the THz radiation. The photoinduced changes to the THz transmission can also be appreciated as a shift in the THz peak in the time domain (see Figure S21, Supporting Information). While no significant shift can be perceived in the bulk material, in the case of the NCs, the THz transmission peak slightly shifts to earlier times after photoexcitation, indicating a decrease in refractive

index in the THz region in the presence of photogenerated charge carriers. It is important to highlight that the experiments were carried out at comparable charge-carrier densities ($\approx 10^{17}$ cm⁻³) in both bulk and NCs. Photoinduced changes to the lattice response to the THz radiation have been previously observed in lead halide perovskites,^[58] and can be indicative of the existence of a photoinduced modification of the vibrational properties. In other words, the presence of charge carriers has an effect on the lattice phonon modes, changing either the phonon oscillator strengths or shifting the resonance frequencies in relation to the ground state distribution.

The more pronounced modulations in the THz photoconductivity spectra of NCs as opposed to the bulk film are likely related to the stronger coupling of THz radiation to the lattice (as a result of higher absorption coefficients or distinct selection rules) observed in the dark absorption of NCs in the THz range. Additionally, the impact of photogenerated charges on the THz refractive index in NCs indicates stronger coupling between the lattice and charge carriers compared to the bulk perovskite. We could also confirm that these modulations appear in the photoconductivity spectra immediately after photoexcitation and persist for at least several picoseconds (see Figure S23, Supporting Information). Such a fast response is counterevidence of the role of photostriction in the modulations, as the lattice reorganization would be expected to occur over longer timescales.^[59–61]

It is worth noting that the μ values obtained from the OPTP measurements (Figure 3) are calculated from the frequency averaged $\Delta T/T$ signal (for details, see Section 3, Supporting Information). This shows that performing and interpreting THz measurements on these materials require care. While the evidence of carrier localization on the low-frequency side of the THz photoconductivity and the increasing μ with increasing crystal size are reliable observations, the absolute values reported are likely affected by such modulations in the intensity of the $\Delta T_{THz}/T_{THz}$ signal.

The contrast between bulk and NC mobility values and photoconductivity spectra illustrates two important points concerning charge transport in these systems. One is the localization of charge carriers within nanoscale crystals, observed even after annealing. Such localization effects limit the charge transport in the THz range (i.e., on picosecond timescales) and indicates that long range conductivity relies on interparticle hopping. However, localization may need to be tolerated in particular in applications for which optoelectronic properties arising from the nanocrystalline dimensions are important, as for example in light-emitting diodes. The second point is the distinct vibrational properties of colloiddally synthesized NCs, which are reflected in the photoconductivity spectra in the form of strong modulations. As shown in Section 2.2, the phonon absorption spectra of NCs are blue-shifted and the coupling of THz radiation to the lattice is twice as strong as in the bulk. Such differences are likely related to the reduced size, increased surface-to-volume ratio, and the lattice expansion in colloidal NCs. The distinct coupling of THz radiation to optical phonons in colloidal NCs can be an indication of fundamental differences in optoelectronic properties with respect to the bulk, in addition to the charge-carrier localization effects. In particular, the blue-shift of the THz spectra can result from more efficient

coupling of light to specific modes of the lattice due to reduced size or orientation. Alternatively, it can also indicate a higher frequency of the phonon modes, which could suggest higher fundamental upper limits for the charge-carrier mobility with respect to that of the bulk.^[45] However, further work is required to investigate in details how the structural and vibrational properties impact the charge-carrier mobility in perovskite NCs.

3. Conclusion

In summary, we have investigated the optoelectronic properties of bulk CsPbBr₃ and colloiddally synthesized NCs in the weak confinement regime (6, 7.5, and 10 nm). We demonstrate how the structural, vibrational, and charge transport properties of NC films deviate from the bulk material and how these are affected by the crystal size. In addition to wider band gaps and higher charge-carrier recombination rates resulting from confinement effects, we also observed a lattice expansion and distinct phonon spectra in the NCs compared to the bulk, which is likely related both to the reduced crystal size and to the crystal formation dynamics during colloidal synthesis in contrast to spin-coating methods. The phonon absorption spectra in the THz region of the NCs show a blue shift, broadening and higher effective relative absorption coefficients with respect to those of the bulk material. In addition to these differences in the dark spectra, we report a photoinduced modification of the phonon modes that can be seen as strong modulations on the photoexcited THz spectra, superimposed with the photoconductivity response. We also report an increase of the effective charge-carrier mobility with increasing crystal size and no dependence on the nature of the ligands or on film annealing. The obtained values for charge-carrier mobility and the shape of the photoconductivity spectra in the THz region demonstrate that the THz probe is sensitive to localized phenomena and that the carrier motion in these nanocrystalline materials is dominated by backscattering. Thus, the long-range photoconductivity of thin films made from NC inks depends on the competition between interparticle hopping and the enhanced recombination rates within NCs. This understanding of charge-carrier dynamics and transport represent an important step towards the optimization of nanocrystalline perovskite thin films for specific optoelectronic applications. In particular, light-emitting applications based on NCs may benefit from films in which NCs retain their mostly intra-particle optoelectronics properties, as investigated here, while photovoltaic applications may be better served by sintered NC films that approach bulk properties. Our findings, therefore, provide valuable information that will guide further fundamental research on perovskite NCs for specific applications.

Supporting Information

Supporting Information is available from the Wiley Online Library or from the author.

Acknowledgements

The authors gratefully acknowledge support from the Engineering and Physical Sciences Research Council (EPSRC) and the European

Union's Horizon 2020 research and innovation programme under the Marie Skłodowska-Curie grant agreement number 675867 (INFORM). S.G.M. and A.J.R. thank EPSRC Prosperity Partnership (EP/S004947/1) and A.J.R. thanks EPSRC SPACE (EP/M015254/2). L.M.H. thanks the Alexander-von-Humboldt Foundation for a Friedrich-Wilhelm-Bessel Research Award.

Conflict of Interest

The authors declare no conflict of interest.

Keywords

charge-carrier dynamics, nanocrystals, perovskites

Received: November 27, 2019

Revised: January 10, 2020

Published online:

- [1] L. Protesescu, S. Yakunin, M. I. Bodnarchuk, F. Krieg, R. Caputo, C. H. Hendon, R. X. Yang, A. Walsh, M. V. Kovalenko, *Nano Lett.* **2015**, *15*, 3692.
- [2] S. Yakunin, L. Protesescu, F. Krieg, M. I. Bodnarchuk, G. Nedelcu, M. Humer, G. De Luca, M. Fiebig, W. Heiss, M. V. Kovalenko, *Nat. Commun.* **2015**, *6*, 8056.
- [3] N. Wang, L. Cheng, R. Ge, S. Zhang, Y. Miao, W. Zou, C. Yi, Y. Sun, Y. Cao, R. Yang, Y. Wei, Q. Guo, Y. Ke, M. Yu, Y. Jin, Y. Liu, Q. Ding, D. Di, L. Yang, G. Xing, H. Tian, C. Jin, F. Gao, R. H. Friend, J. Wang, W. Huang, *Nat. Photonics* **2016**, *10*, 699.
- [4] Q. A. Akkerman, M. Gandini, F. Di Stasio, P. Rastogi, F. Palazon, G. Bertoni, J. M. Ball, M. Prato, A. Petrozza, L. Manna, *Nat. Energy* **2017**, *2*, 16194.
- [5] F. Krieg, S. T. Ochsenbein, S. Yakunin, S. ten Brinck, P. Aellen, A. Süess, B. Clerc, D. Guggisberg, O. Nazarenko, Y. Shynkarenko, S. Kumar, C.-J. Shih, I. Infante, M. V. Kovalenko, *ACS Energy Lett.* **2018**, *3*, 641.
- [6] J. Li, L. Xu, T. Wang, J. Song, J. Chen, J. Xue, Y. Dong, B. Cai, Q. Shan, B. Han, H. Zeng, *Adv. Mater.* **2017**, *29*, 1603885.
- [7] D. V. Talapin, J.-S. Lee, M. V. Kovalenko, E. V. Shevchenko, *Chem. Rev.* **2010**, *110*, 389.
- [8] L. M. Wheeler, E. M. Sanehira, A. R. Marshall, P. Schulz, M. Suri, N. C. Anderson, J. A. Christians, D. Nordlund, D. Sokaras, T. Kroll, S. P. Harvey, J. J. Berry, L. Y. Lin, J. M. Luther, *J. Am. Chem. Soc.* **2018**, *140*, 10504.
- [9] S. Dastidar, D. A. Egger, L. Z. Tan, S. B. Cromer, A. D. Dillon, S. Liu, L. Kronik, A. M. Rappe, A. T. Fafarman, *Nano Lett.* **2016**, *16*, 3563.
- [10] C. Wehrenfennig, G. E. Eperon, M. B. Johnston, H. J. Snaith, L. M. Herz, *Adv. Mater.* **2014**, *26*, 1584.
- [11] S. G. Motti, T. Crothers, R. Yang, Y. Cao, R. Li, M. B. Johnston, J. Wang, L. M. Herz, *Nano Lett.* **2019**, *19*, 3953.
- [12] L. M. Herz, *ACS Energy Lett.* **2017**, *2*, 1539.
- [13] M. B. Johnston, L. M. Herz, *Acc. Chem. Res.* **2016**, *49*, 146.
- [14] C. L. Davies, J. B. Patel, C. Q. Xia, L. M. Herz, M. B. Johnston, *J. Infrared, Millimeter, Terahertz Waves* **2018**, *39*, 1236.
- [15] D. Wang, J. Zhao, B. Chen, C. Zhu, *J. Phys. Condens. Matter* **2008**, *20*, 085212.
- [16] L. Dou, A. B. Wong, Y. Yu, M. Lai, N. Kornienko, S. W. Eaton, A. Fu, C. G. Bischak, J. Ma, T. Ding, N. S. Ginsberg, L.-W. Wang, A. P. Alivisatos, P. Yang, *Science* **2015**, *349*, 1518.
- [17] E. S. Parrott, J. B. Patel, A.-A. Haghghirad, H. J. Snaith, M. B. Johnston, L. M. Herz, *Nanoscale* **2019**, *11*, 14276.

- [18] D. Di, K. P. Musselman, G. Li, A. Sadhanala, Y. Ievskaya, Q. Song, Z.-K. Tan, M. L. Lai, J. L. MacManus-Driscoll, N. C. Greenham, R. H. Friend, *J. Phys. Chem. Lett.* **2015**, *6*, 446.
- [19] L. Polavarapu, B. Nickel, J. Feldmann, A. S. Urban, *Adv. Energy Mater.* **2017**, *7*, 1700267.
- [20] T. W. Jones, A. Osherov, M. Alsari, M. Sponseller, B. C. Duck, Y.-K. Jung, C. Setzens, F. Niroui, R. Brenes, C. V. Stan, Y. Li, M. Abdi-Jalebi, N. Tamura, J. E. Macdonald, M. Burghammer, R. H. Friend, V. Bulović, A. Walsh, G. J. Wilson, S. Lilliu, S. D. Stranks, *Energy Environ. Sci.* **2019**, *12*, 596.
- [21] P. Cottingham, R. L. Brutchey, *Chem. Commun.* **2016**, 5246, 5246.
- [22] F. Bertolotti, L. Protesescu, M. V. Kovalenko, S. Yakunin, A. Cervellino, S. J. L. Billinge, M. W. Terban, J. S. Pedersen, N. Masciocchi, A. Guagliardi, *ACS Nano* **2017**, *11*, 3819.
- [23] C. C. Stoumpos, C. D. Malliakas, J. A. Peters, Z. Liu, M. Sebastian, J. Im, T. C. Chasapis, A. C. Wibowo, D. Y. Chung, A. J. Freeman, B. W. Wessels, M. G. Kanatzidis, *Cryst. Growth Des.* **2013**, *13*, 2722.
- [24] W. H. Hall, *Proc. Phys. Soc., Sect. A* **1949**, *62*, 741.
- [25] P. M. Diehm, P. Ágoston, K. Albe, *ChemPhysChem* **2012**, *13*, 2443.
- [26] S. Tsunekawa, K. Ishikawa, Z.-Q. Li, Y. Kawazoe, A. Kasuya, *Phys. Rev. Lett.* **2000**, *85*, 3440.
- [27] A. Swarnkar, A. R. Marshall, E. M. Sanehira, B. D. Chernomordik, D. T. Moore, J. A. Christians, T. Chakrabarti, J. M. Luther, *Science* **2016**, *354*, 92.
- [28] L. Saviot, B. Champagnon, E. Duval, I. A. Kudriavtsev, A. I. Ekimov, *J. Non-Cryst. Solids* **1996**, *197*, 238.
- [29] H. Richter, Z. P. Wang, L. Ley, *Solid State Commun.* **1981**, *39*, 625.
- [30] M. A. Pérez-Osorio, R. L. Milot, M. R. Filip, J. B. Patel, L. M. Herz, M. B. Johnston, F. Giustino, *J. Phys. Chem. C* **2015**, *119*, 25703.
- [31] M. A. Pérez-Osorio, Q. Lin, R. T. Phillips, R. L. Milot, L. M. Herz, M. B. Johnston, F. Giustino, *J. Phys. Chem. C* **2018**, *122*, 21703.
- [32] V. I. Klimov, *Science* **2000**, *287*, 1011.
- [33] M. Li, S. Bhaumik, T. W. Goh, M. S. Kumar, N. Yantara, M. Grätzel, S. Mhaisalkar, N. Mathews, T. C. Sum, *Nat. Commun.* **2017**, *8*, 14350.
- [34] Y. Yamada, T. Nakamura, M. Endo, A. Wakamiya, Y. Kanemitsu, *J. Am. Chem. Soc.* **2014**, *136*, 11610.
- [35] S. D. Stranks, V. M. Burlakov, T. Leijtens, J. M. Ball, A. Gorieli, H. J. Snaith, *Phys. Rev. Appl.* **2014**, *2*, 034007.
- [36] S. G. Motti, M. Gandini, A. J. Barker, J. M. Ball, A. R. Srimath Kandada, A. Petrozza, *ACS Energy Lett.* **2016**, *1*, 726.
- [37] V. K. Ravi, P. K. Santra, N. Joshi, J. Chugh, S. K. Singh, H. Rensmo, P. Ghosh, A. Nag, *J. Phys. Chem. Lett.* **2017**, *8*, 4988.
- [38] T. W. Crothers, R. L. Milot, J. B. Patel, E. S. Parrott, J. Schlipf, P. Müller-Buschbaum, M. B. Johnston, L. M. Herz, *Nano Lett.* **2017**, *17*, 5782.
- [39] Y. Yamada, T. Yamada, L. Q. Phuong, N. Maruyama, H. Nishimura, A. Wakamiya, Y. Murata, Y. Kanemitsu, *J. Am. Chem. Soc.* **2015**, *137*, 10456.
- [40] L. M. Pazos-Outon, M. Szumilo, R. Lamboll, J. M. Richter, M. Crespo-Quesada, M. Abdi-Jalebi, H. J. Beeson, M. Vruini, M. Alsari, H. J. Snaith, B. Ehrler, R. H. Friend, F. Deschler, *Science* **2016**, *351*, 1430.
- [41] Y. Li, T. Ding, X. Luo, Z. Chen, X. Liu, X. Lu, K. Wu, *Nano Res.* **2019**, *12*, 619.
- [42] J. A. Castañeda, G. Nagamine, E. Yassitepe, L. G. Bonato, O. Voznyy, S. Hoogland, A. F. Nogueira, E. H. Sargent, C. H. B. Cruz, L. A. Padilha, *ACS Nano* **2016**, *10*, 8603.
- [43] I. Robel, R. Gresback, U. Kortshagen, R. D. Schaller, V. I. Klimov, *Phys. Rev. Lett.* **2009**, *102*, 177404.
- [44] P. Tiwana, P. Docampo, M. B. Johnston, H. J. Snaith, L. M. Herz, *ACS Nano* **2011**, *5*, 5158.
- [45] S. Poncé, M. Schlipf, F. Giustino, *ACS Energy Lett.* **2019**, *4*, 456.
- [46] M. Sendner, P. K. Nayak, D. A. Egger, S. Beck, C. Müller, B. Epling, W. Kowalsky, L. Kronik, H. J. Snaith, A. Pucci, R. Lovrinčić, *Mater. Horiz.* **2016**, *3*, 613.
- [47] G. M. Turner, M. C. Beard, C. A. Schmuttenmaer, *J. Phys. Chem. B* **2002**, *106*, 11716.
- [48] M. C. Beard, G. M. Turner, C. A. Schmuttenmaer, *Nano Lett.* **2002**, *2*, 983.
- [49] J. Lloyd-Hughes, T.-I. Jeon, *J. Infrared, Millimeter, Terahertz Waves* **2012**, *33*, 871.
- [50] H. J. Joyce, J. L. Boland, C. L. Davies, S. A. Baig, M. B. Johnston, *Semicond. Sci. Technol.* **2016**, *31*, 103003.
- [51] R. L. Milot, G. E. Eperon, H. J. Snaith, M. B. Johnston, L. M. Herz, *Adv. Funct. Mater.* **2015**, *25*, 6218.
- [52] C. L. Davies, J. Borchert, C. Q. Xia, R. L. Milot, H. Kraus, M. B. Johnston, L. M. Herz, *J. Phys. Chem. Lett.* **2018**, *9*, 4502.
- [53] M. V. Kovalenko, L. Protesescu, M. I. Bodnarchuk, *Science* **2017**, *358*, 745.
- [54] J. Li, L. Luo, H. Huang, C. Ma, Z. Ye, J. Zeng, H. He, *J. Phys. Chem. Lett.* **2017**, *8*, 1161.
- [55] K. Zheng, Q. Zhu, M. Abdellah, M. E. Messing, W. Zhang, A. Generalov, Y. Niu, L. Ribaud, S. E. Canton, T. Pullerits, *J. Phys. Chem. Lett.* **2015**, *6*, 2969.
- [56] K. Tanaka, T. Takahashi, T. Ban, T. Kondo, K. Uchida, N. Miura, *Solid State Commun.* **2003**, *127*, 619.
- [57] N. Smith, *Phys. Rev. B* **2001**, *64*, 155106.
- [58] Y. Lan, B. J. Dringoli, D. A. Valverde-Chávez, C. S. Ponceca, M. Sutton, Y. He, M. G. Kanatzidis, D. G. Cooke, *Sci. Adv.* **2019**, *5*, eaaw5558.
- [59] Y. Zhou, L. You, S. Wang, Z. Ku, H. Fan, D. Schmidt, A. Ruydy, L. Chang, L. Wang, P. Ren, L. Chen, G. Yuan, L. Chen, J. Wang, *Nat. Commun.* **2016**, *7*, 11193.
- [60] T.-C. Wei, H.-P. Wang, T.-Y. Li, C.-H. Lin, Y.-H. Hsieh, Y.-H. Chu, J.-H. He, *Adv. Mater.* **2017**, *29*, 1701789.
- [61] H. Tsai, R. Asadpour, J.-C. Blancon, C. C. Stoumpos, O. Durand, J. W. Strzalka, B. Chen, R. Verduzco, P. M. Ajayan, S. Tretiak, J. Even, M. A. Alam, M. G. Kanatzidis, W. Nie, A. D. Mohite, *Science* **2018**, *360*, 67.